



AIAA 2002–5548

**Multi-Point and Multi-Objective
Aerodynamic Shape Optimization**

Marian Nemec, David W. Zingg,
*University of Toronto Institute for Aerospace Studies
4925 Dufferin Street, Toronto, ON, M3H 5T6, Canada*

and

Thomas H. Pulliam
*NASA Ames Research Center
Moffett Field, CA 94035, USA*

**9th AIAA/ISSMO Symposium on
Multidisciplinary Analysis and Optimization
Sept. 4–6, 2002/Atlanta, Georgia**

Multi-Point and Multi-Objective Aerodynamic Shape Optimization

Marian Nemec,^{*} David W. Zingg,[†]

*University of Toronto Institute for Aerospace Studies
4925 Dufferin Street, Toronto, ON, M3H 5T6, Canada*

and

Thomas H. Pulliam[‡]

*NASA Ames Research Center
Moffett Field, CA 94035, USA*

A Newton–Krylov algorithm is presented for the aerodynamic optimization of single- and multi-element airfoil configurations. The flow is governed by the compressible Navier–Stokes equations in conjunction with a one-equation turbulence model. The preconditioned generalized minimum residual method is applied to solve the discrete-adjoint equation, leading to a fast computation of accurate objective function gradients. Optimization constraints are enforced through a penalty formulation, and the resulting unconstrained problem is solved via a quasi-Newton method. Design examples include lift-enhancement and multi-point lift-constrained drag minimization problems. Furthermore, the new algorithm is used to compute a Pareto front for a multi-objective problem, and the results are validated using a genetic algorithm. Overall, the new algorithm provides an efficient and robust approach for addressing the issues of complex aerodynamic design.

Introduction

CURRENT algorithms for the solution of the two-dimensional Navier–Stokes equations provide reasonable predictions of aerodynamic performance for complex airfoil geometries.¹ Although still a subject of research, the solvers are becoming accurate, robust, and computationally inexpensive. For the solution of the aerodynamic shape optimization problem, the validated solvers are typically combined with numerical optimization methods, for example gradient-based methods and search methods. Perhaps the most popular approach for the computation of the objective function gradient is the adjoint method,^{2–7} since its cost is virtually independent of the number of design variables. Search methods, such as genetic algorithms,^{8–10} are not as efficient as gradient-based methods; however, they do not require the calculation of the gradient and they may be advantageous for complex, non-smooth, multi-objective problems.

A classic aerodynamic application of numerical optimization methods is the design of cruise configurations for transonic flow,^{11–13} and recently, for supersonic

flow.^{14,15} Furthermore, the application of these methods to the design of high-lift configurations is also an active area of research.^{16–20} An efficient high-lift configuration can significantly improve the aerodynamic performance of an aircraft, as well as provide weight savings and reductions in mechanical complexity.²¹ Therefore, in order to address all aspects of aerodynamic design, a practical algorithm requires effective capabilities for optimization using multiple objectives, which may include multidisciplinary interactions,²² and multiple operating points.

A well-known approach for solving multi-point and multi-objective problems is the weighted-sum method. Detailed examples of this method for the multi-point design of cruise configurations are provided by Drela.²³ The main shortcoming of this method is the selection of appropriate design points and their associated weights. Huyse and Lewis²⁴ recently introduced a promising formulation based on a statistical approach that avoids this difficulty.

In Ref. 25, we presented an accurate and efficient algorithm for the calculation of the gradient via the discrete-adjoint approach. The adjoint equation is solved using the preconditioned generalized minimum residual (GMRES) Krylov subspace method.²⁶ Furthermore, the same preconditioned GMRES method is also used within a Newton–Krylov flow solver for fast solution of the flowfield equations. Overall, the gradient is obtained in just one-fifth to one-half of the

^{*}PhD Candidate, marian@oddjob.utoronto.ca

[†]Professor, Senior Member AIAA, <http://goldfinger.utoronto.ca/~dwz/>

[‡]Senior Research Scientist, Associate Fellow AIAA, tpulliam@mail.arc.nasa.gov

Copyright © 2001 by M. Nemec and D. W. Zingg. Published by the American Institute of Aeronautics and Astronautics, Inc. with permission.

time required for a warm-started flow solution.

The objectives of this paper are to extend and apply the Newton–Krylov algorithm presented in Ref. 25 to the following three areas of aerodynamic design:

1. Optimization of high-lift configurations
2. Multi-objective optimization
3. Multi-point optimization

Factors under consideration include efficiency of the optimization, design robustness, global and local minima, and the computation of Pareto fronts. A genetic algorithm, presented in Ref. 10, is used to validate the multi-objective results.

Problem Formulation

The aerodynamic shape optimization problem consists of determining values of design variables X , such that the objective function \mathcal{J} is minimized

$$\min_X \mathcal{J}(X, Q) \quad (1)$$

subject to constraint equations C_j :

$$C_j(X, Q) \leq 0 \quad j = 1, \dots, N_c \quad (2)$$

where the vector Q denotes the conservative flowfield variables and N_c denotes the number of constraint equations. The flowfield variables are forced to satisfy the governing flowfield equations, \mathcal{F} , within a feasible region of the design space Ω :

$$\mathcal{F}(X, Q) = 0 \quad \forall X \in \Omega \quad (3)$$

which implicitly defines $Q = f(X)$.

For the examples under consideration here, the objective function is given by

$$\mathcal{J} = \begin{cases} \omega_L \left(1 - \frac{C_L}{C_L^*}\right)^2 + \omega_D \left(1 - \frac{C_D}{C_D^*}\right)^2 & \text{if } C_D > C_D^* \\ \omega_L \left(1 - \frac{C_L}{C_L^*}\right)^2 & \text{otherwise} \end{cases} \quad (4)$$

where C_D^* and C_L^* represent the target drag and lift coefficients, respectively. The weights ω_D and ω_L are user specified constants. This objective can be used for both lift-enhancement and lift-constrained drag minimization problems. The weighted-sum method is used for multi-point optimization problems:

$$\mathcal{J}_m = \sum_{i=1}^{N_m} w_i \mathcal{J}_i \quad (5)$$

where N_m denotes the number of design points (typically Mach numbers), and w_i represents a user assigned weight to each design point.

The design variables are based on a B-spline parameterization^{25, 27} of the airfoil. An example is shown in

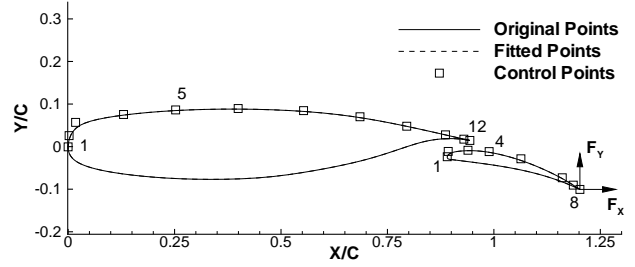


Fig. 1 B-spline curves and flap translation design variables

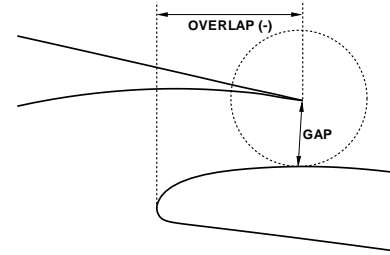


Fig. 2 Definition of gap and overlap distances

Fig. 1, where a B-spline curve is fitted over the upper surface of the main element, and also the upper surface of the flap for the NLR 7301 configuration.²⁸ The vertical coordinates of the B-spline control points are used as design variables. Depending on the problem of interest, additional design variables may include the angle of attack, and the horizontal and vertical translation associated with each high-lift element in multi-element configurations, labeled as F_x and F_y in Fig. 1. The horizontal and vertical translation design variables control the gap and overlap distances in the slot region of the airfoil, as defined in Fig. 2.

The constraint equations, Eq. 2, represent airfoil thickness constraints that are used to ensure feasible designs. The constraints are given by

$$h^*(z_j) - h(z_j) \leq 0 \quad (6)$$

where $h^*(z_j)$ represents the minimum allowable thickness at location z_j expressed as a fraction of the airfoil's chord. For multi-element configurations, it is also necessary to constrain the gap and overlap distances. These constraints are required in order to prevent collisions among the elements and to ensure a reasonable computational grid.

The governing flow equations are the compressible two-dimensional thin-layer Navier–Stokes equations in generalized coordinates:

$$\frac{\partial \hat{E}(X, \hat{Q})}{\partial \xi} + \frac{\partial \hat{F}(X, \hat{Q})}{\partial \eta} = Re^{-1} \frac{\partial \hat{S}(X, \hat{Q})}{\partial \eta} \quad (7)$$

where $\hat{Q} = J^{-1}Q = J^{-1}[\rho, \rho u, \rho v, e]^T$ is the vector of conservative dependent state variables, ξ and η are the streamwise and normal generalized coordinates,

respectively, and J is the Jacobian of the coordinate transformation from Cartesian coordinates. Vectors \hat{E} and \hat{F} represent the convective flux vectors, the viscous flux vector is given by \hat{S} , and Re denotes the Reynolds number. Sutherland's law is used to determine the laminar viscosity. The equations are in non-dimensional form. For further details, see Ref. 29. The turbulent viscosity is modeled with the Spalart–Allmaras turbulence model.³⁰ All cases considered in this study are assumed to be fully turbulent, and therefore, the laminar-turbulent trip terms are not used.

Numerical Method

The aerodynamic shape optimization problem defined by Eqs. 1–3 is cast as an unconstrained problem. This is accomplished by lifting the side constraints, Eq. 2, into the objective function \mathcal{J} using a penalty method. Furthermore, the constraint imposed by the flowfield equations, Eq. 3, is satisfied at every point within the feasible design space, and consequently these equations do not explicitly appear in the formulation of the optimization problem.

The unconstrained problem is solved using the BFGS quasi-Newton method in conjunction with a backtracking line search.^{25, 31} At each step of the line search, the objective function value and gradient are required in order to construct a local cubic interpolant. Note that the optimization problem is based on the discrete form of the flowfield equations. Using the discrete approach, we expect the gradient to vanish at the optimum solution. In the following sections, we present the formulation for the penalized objective function, as well as the algorithms used for the flowfield evaluation (objective function value), the gradient evaluation, and the grid-perturbation strategy.

Objective with Constraints

A penalty method is used to combine the objective function with the constraint equations. For example, the formulation for the thickness constraints is given by

$$\mathcal{J} = \mathcal{J}_O + \omega_T \sum_{j=1}^{N_c} C_j \quad (8)$$

where \mathcal{J}_O refers to Eq. 4 and ω_T is a user specified constant. The constraint equations C_j , based on Eq. 6, are cast using a quadratic penalty term:

$$C_j = \begin{cases} [1 - h(z_j)/h^*(z_j)]^2 & \text{if } h(z_j) < h^*(z_j) \\ 0 & \text{otherwise} \end{cases} \quad (9)$$

A similar formulation is used to enforce the lower and upper bounds for the gap and overlap distances.

Flowfield Evaluation

The spatial discretization of the flowfield equations, Eq. 7, is the same as that used in ARC2D²⁹ and TORNADO³² for multi-block H-topology grids. The discretization consists of second-order centered-difference

operators with second- and fourth-difference scalar artificial dissipation. The Spalart–Allmaras turbulence model is discretized as described in Refs. 30 and 33. Overall, the spatial discretization leads to a nonlinear system of equations:

$$R(X, \hat{Q}) = 0 \quad (10)$$

where $\hat{Q} = J^{-1}Q = J^{-1}[\rho, \rho u, \rho v, e, \tilde{v}]^T$ is the new vector of conservative dependent state variables, and the turbulence model equation is scaled by J^{-1} . On multi-block grids, the block interfaces are overlapped in the streamwise direction and averaged in the normal direction. Two columns of halo points are used at the streamwise block interfaces. Although R is written as a function of the design variables, we emphasize that during a flowfield solution the design variables, and consequently the computational grid, are constants.

Eq. 10 is solved in a fully-coupled manner, where convergence to steady state is achieved using the preconditioned GMRES algorithm in conjunction with an inexact-Newton strategy.^{25, 34} The main components include matrix-free GMRES(40) and a block-fill incomplete LU (BFILU) preconditioner. The matrix-vector products required at each GMRES iteration are formed with first-order finite-differences. Right preconditioning is used, and the preconditioner is based on an approximate-flow-Jacobian matrix. The level of fill for most cases is 2 [BFILU(2)], but difficult multi-element cases may require BFILU(4). The approximate-factorization algorithm of ARC2D in diagonal form^{29, 32} in conjunction with a subiteration scheme³⁰ for the turbulence model equation is used to reduce the initial residual by three orders of magnitude in order to avoid Newton startup problems.

The approximate-flow-Jacobian matrix used for the preconditioner is identical to the flow-Jacobian matrix, $\partial R / \partial Q$, except for the treatment of the artificial-dissipation coefficients.²⁵ Hence, the preconditioner contains the contributions from all components of the residual vector, namely inviscid and viscous fluxes, boundary conditions, block interfaces, and the turbulence model. The artificial-dissipation coefficients, which include the spectral radius and the pressure switch, are assumed to be constant with respect to the flowfield variables. Furthermore, the preconditioning matrix is formed with only second-difference dissipation, but the second-difference coefficient is combined with the fourth-difference coefficient as follows,

$$d_l^{(2)} = d_r^{(2)} + \phi d_r^{(4)} \quad (11)$$

where the subscript r denotes the contribution from the right-hand side, and the subscript l denotes the resulting left-hand side value used in forming the preconditioner. This modification does not affect the steady-state solution. Fast convergence is obtained with the value of ϕ set to 6.0, which has been determined through numerical experiments.

Eq. 11 improves the diagonal dominance of the preconditioning matrix and reduces the work and storage requirements of the incomplete factorization. This approach is similar to the ‘diagonal shift’ strategy suggested by Chow and Saad.³⁵ The present preconditioning matrix is a compromise between a preconditioner based on a first-order upwind discretization of the flowfield equations and a preconditioner based on the actual second-order discretization. This novel ‘intermediate’ preconditioner is significantly more effective than either of these more commonly used approaches.

Gradient Evaluation

Using the discrete-adjoint method, the expression for the gradient, \mathcal{G} , of the objective function, $\mathcal{J}[X, Q(X)]$, is given by

$$\mathcal{G} = \frac{d\mathcal{J}}{dX} = \frac{\partial\mathcal{J}}{\partial X} - \psi^T \frac{\partial R}{\partial X} \quad (12)$$

where we reduce the vector of design variables, X , to a scalar in order to clearly distinguish between partial and total derivatives. For problems with multiple design variables, it may be helpful to note that \mathcal{G} and $\partial\mathcal{J}/\partial X$ are $[1 \times N_D]$ row vectors, ψ is a $[N_F \times 1]$ column vector, and $\partial R/\partial X$ is a $[N_F \times N_D]$ matrix, where N_D represents the number of design variables and N_F represents the number of flowfield variables. We assume that the implicit function $Q(X)$ defined by Eq. 10 is sufficiently smooth even in the presence of flow discontinuities such as shock waves.^{36–38}

The vector ψ represents adjoint variables, which are given by the adjoint equation:

$$\frac{\partial R}{\partial Q}^T \psi = \frac{\partial\mathcal{J}}{\partial Q}^T \quad (13)$$

This is a large, sparse, linear system of equations that is independent of the design variables. The GMRES strategy from the flow solver is adopted to solve the adjoint equation. Fast solutions are obtained with GMRES(85) and for the preconditioning matrix we use BFILU(6) and $\phi = 3.0$. Multi-element airfoil cases with complex flowfields may require $\phi = 6.0$, which improves the robustness of the adjoint solver. Due to the transpose on the left-hand-side of Eq. 13, the matrix-free approach used in the flow solver is not possible for the adjoint equation. The flow-Jacobian matrix is stored explicitly, where we include the contribution from the spectral radius, but we treat the pressure switch associated with the artificial dissipation scheme as a constant.

The remaining terms in Eqs. 12 and 13, namely the objective function sensitivities $\partial\mathcal{J}/\partial X$ and $\partial\mathcal{J}/\partial Q$, as well as the residual sensitivity $\partial R/\partial X$, are evaluated using centered differences. The use of centered differences for the evaluation of the partial derivative terms is not computationally expensive. For example,

the centered-difference formula for the residual sensitivities is given by

$$\frac{\partial R}{\partial X_i} = \frac{R(X + he_i, Q) - R(X - he_i, Q)}{2h} \quad (14)$$

where

$$h = \max(\epsilon \cdot |X_i|, 1 \times 10^{-8}) \quad (15)$$

and $i = 1, \dots, N_D$. The i th unit vector is denoted by e_i , and a typical value of ϵ is 1×10^{-5} . It is important to realize that Eq. 14 involves two evaluations of only the residual vector per design variable and *not* two flowfield solutions. Note that the evaluation of residual sensitivities includes the evaluation of grid sensitivities, since the design variables do not explicitly appear in the residual equations except for the angle of attack design variable.

Grid-Movement Strategy

As the shape and position of an airfoil evolve during the optimization process, the location of the grid nodes is adjusted from the baseline configuration to conform to the new configuration. In Ref. 25, we use an algebraic grid-perturbation strategy that preserves the distance to the outer boundary and relocates the grid nodes in the normal direction proportional to the distance from the airfoil boundary. When the optimization problem involves the horizontal and vertical translation of a slat or a flap, the use of this strategy can result in significantly skewed grid cells near the boundary.

In order to improve the quality of the modified multi-block grids, we present a new grid-perturbation strategy given by

$$y_k^{\text{new}} = y_k^{\text{old}} + \frac{\Delta y}{2} [1 + \cos(\pi S_k)] \quad (16)$$

where Δy represents the airfoil shape change. S_k is the normalized arclength distance given by

$$S_k = \frac{1}{L_g} \sum_{i=2}^k L_i \quad k = 2, \dots, k_{\text{max}} - 1 \quad (17)$$

where $S_1 = 0$, L_i is the length of a segment between nodes k and $k - 1$, and L_g is the grid-line length from the body to the outer boundary.

Results and Discussion

Before presenting aerodynamic design examples, we carefully validate the performance of the flow solver and the gradient computation algorithm. C-topology grids for single-element configurations consist of 257×57 nodes, where the distance to the outer boundary is 24 chords, the off-wall spacing is 2×10^{-6} chords, the leading-edge clustering is 5×10^{-4} chords and the trailing-edge clustering is 2×10^{-3} chords. For multi-element configurations, the H-topology grids contain

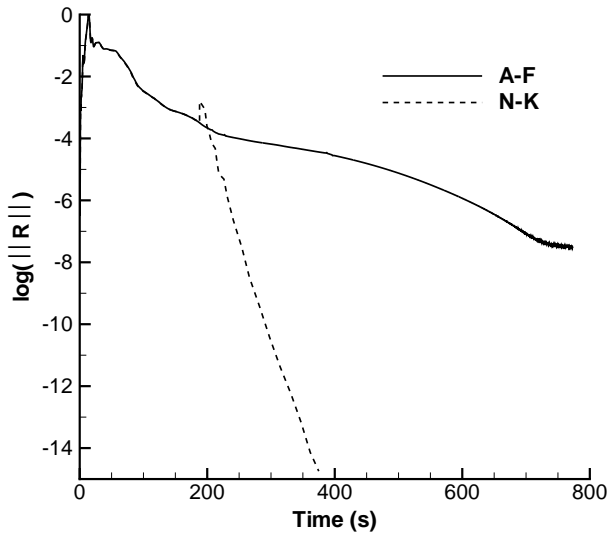


Fig. 3 Flow-solver performance

approximately 31,000 nodes. The off-wall spacing is $2 \times 10^{-6}c$, the distance to the outer boundary is $12c$, the spacing at the grid stagnation points is $2 \times 10^{-5}c$, and the trailing-edge clustering is $2 \times 10^{-3}c$. The reported CPU times are obtained on a 667 MHz Alpha 21264 processor (SPECfp 2000 rating of 562 peak).

Validation

Flow-Solver Performance

A fast solution of the flowfield equations is a critical component of an effective design algorithm, since an evaluation of the objective function is required at each iteration of the optimizer. The performance of the flow solver is examined for the NLR 7301 configuration at $M_\infty = 0.25$, $\alpha = 8^\circ$ and $Re = 2.51 \times 10^6$. Fig. 3 shows that the Newton–Krylov flow solver (denoted as NK) is approximately two to three times faster than the approximate-factorization flow solver (denoted as AF). For many cases, this speed-up can be even larger. Initially, the convergence rate of both flow solvers is identical, since approximate-factorization is used as a startup procedure for the Newton–Krylov flow solver.

One of the main difficulties associated with Newton’s method is the startup procedure. The Newton–Krylov flow solver is particularly well suited for the design problem since once we obtain the solution for the initial airfoil shape, we warm-start the remaining flow solves. If the stepsizes during the line-search procedure are sufficiently small, the startup procedure using approximate factorization is not necessary. The warm-started flow solves typically converge in 2/3 of the original flow solve time.

Accuracy and Efficiency of Gradient Computation

Finite-difference gradients provide a benchmark that is used to establish the accuracy of the gradient computation using the adjoint method. A subsonic

Table 1 Gradient accuracy

Design Variable	Finite Difference	Adjoint (% Diff.) ^a
5M	-0.01228	0.02
4F	-0.08533	-0.19
F_x	-0.02591	0.06
F_y	-0.03363	-0.05

$$^a \% \text{ Diff} = (\mathcal{G} - \mathcal{G}_{\text{FD}}) / \mathcal{G}_{\text{FD}} \times 100$$

lift-enhancement problem for the NLR 7301 configuration is considered. During the computation of the finite-difference gradient, the flowfield solution is converged 14 orders of magnitude. The adjoint equation is converged 8 orders of magnitude.

The freestream conditions are $M_\infty = 0.25$, $\alpha = 4^\circ$, and $Re = 2.51 \times 10^6$. We compute the gradient of the objective function, Eq. 4, with respect to control point 5 on the main airfoil (denoted as 5M), control point 4 on the flap (denoted as 4F), and the horizontal and vertical flap displacements (denoted as F_x and F_y , respectively), see Fig. 1. The target drag coefficient, C_D^* , is set equal to the initial drag coefficient, while the target lift coefficient, C_L^* , is set equal to 2.2, which represents a 2.5% increase from the initial value. The values of ω_L and ω_D in Eq. 4 are both set to 1.0 and there are no side constraints. Table 1 shows that there is an excellent agreement between the finite-difference and adjoint gradients.

Fig. 4 compares the convergence history of the adjoint and flowfield equations with respect to CPU time. The time for the formation of the preconditioning matrices is included in Fig. 4.¹ It is necessary to converge the adjoint equation only three orders of magnitude in order to obtain gradients of sufficient accuracy.^{39–41} This level of convergence is achieved in approximately 45 seconds, as shown in Fig. 4. For the flowfield equations, we typically reduce the residual by ten orders of magnitude in order to prevent stalling of the line searches once the solution is close to the optimum. This convergence level is achieved in 245 seconds, and consequently, the gradient is obtained in less than one-fifth of the flow solve time.

Design Examples

Optimization of High-Lift Configurations

The first design example demonstrates the performance of the Newton–Krylov algorithm for the optimization of complex high-lift aerodynamic configurations. This optimization is based on a single operating point and objective function, but we consider the issue of local versus global minima. The goal is to

¹In Fig. 4, the ‘flat step’ in the convergence of the flow solver after a three order-of-magnitude decrease in the residual indicates the formation time of the preconditioner. For the adjoint equation, this time is indicated at the start of the convergence history.

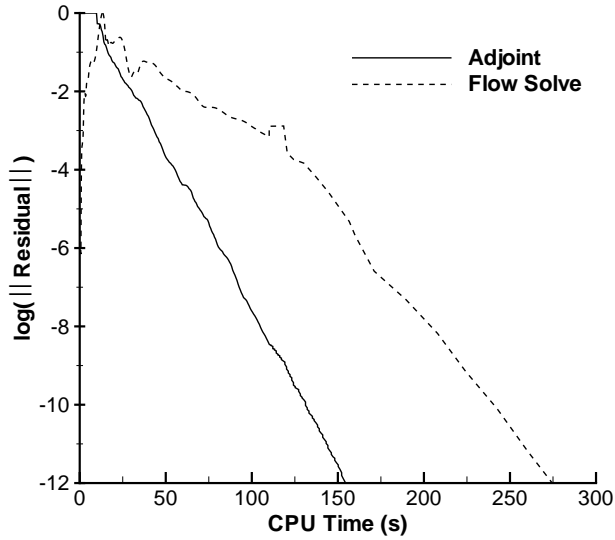


Fig. 4 Comparison of adjoint and flow solve convergence times

determine the optimal gap and overlap distances for the NLR 7301 configuration, such that the modified configuration achieves a higher lift coefficient while maintaining the same (or lower) drag coefficient as the original configuration. The freestream conditions are $M_\infty = 0.25$, $\alpha = 4^\circ$, and $Re = 2.51 \times 10^6$. The initial values of C_L and C_D are 2.145 and 0.04720, respectively. The objective function is given by Eq. 4, where we set $C_L^* = 2.180$ and C_D^* equal to the initial drag coefficient. The weights ω_L and ω_D are set to 1.0. The design variables are the horizontal and vertical displacements of the trailing edge of the flap, as indicated in Fig. 1. The gap and overlap limits are set to $\pm 0.5\%c$ and $\pm 1.0\%c$, respectively, based on the initial configuration. The weight associated with the gap and overlap constraints is set to 0.05.

Table 2 and Fig. 5 summarize the results. Within a few flowfield and gradient evaluations, the flap reaches the maximum allowable overlap distance of approximately $-4.3\%c$, at which point the overlap penalty function becomes active. The optimization converges to the design #1 configuration, shown in Fig. 5. A new grid is generated for this configuration and the corresponding values of C_L and C_D are given in Table 2. The optimization is restarted from the new grid with the same objective function. This procedure is continued until convergence to the final design is obtained (see Fig. 5), where the gap and overlap constraints are no longer active. Note that the drag objective is satisfied for all the designs. Consequently, the optimization is purely attempting to maximize the lift coefficient. Overall, a 1.4% increase in the value of the lift coefficient is obtained. This is achieved by an increased loading on the main element as well as the flap, as shown in Fig. 6.

Example convergence histories for the design #2 and

Table 2 Gap-overlap optimization summary

Design	C_L	C_D	G^a	O^b
NLR 7301	2.145	0.04720	2.40	-5.31
#1	2.165	0.04687	1.99	-4.28
#2	2.173	0.04677	1.95	-3.30
Final	2.175	0.04675	2.02	-2.68
Target	2.180	≤ 0.0472		

^a Gap ($\%c$)

^b Overlap ($\%c$)

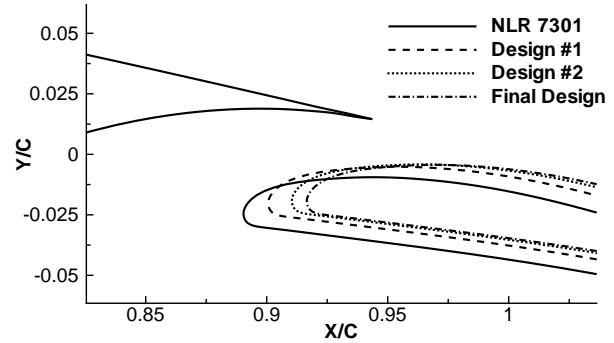


Fig. 5 Flap position summary

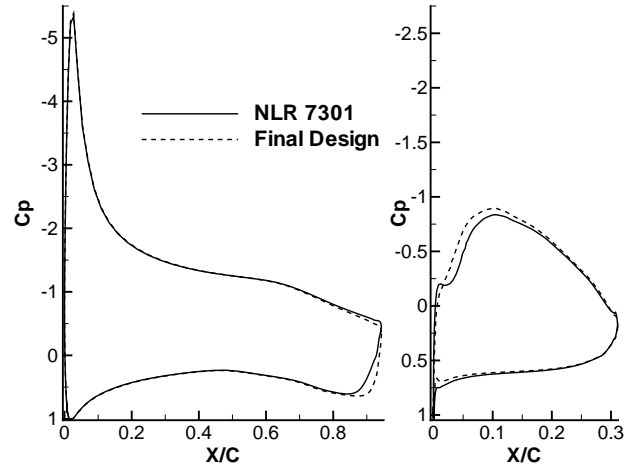


Fig. 6 C_p distribution for main element and flap

final configurations are shown in Fig. 7. The oscillations in the L_2 norm of the gradient for design #2 are due to the presence of the gap and overlap constraints. The norm of the gradient is reduced by several orders of magnitude, which indicates that the optimization converged to a local minimum.

Given that the target value of the lift coefficient is not achieved at the final design configuration (see Table 2), it is somewhat surprising that further design improvements cannot be realized by further extending the effective chord of the configuration. The convergence of the gradient in Fig. 7 indicates that a local optimum has been found, but a global optimum is not guaranteed. In order to verify the uniqueness of the

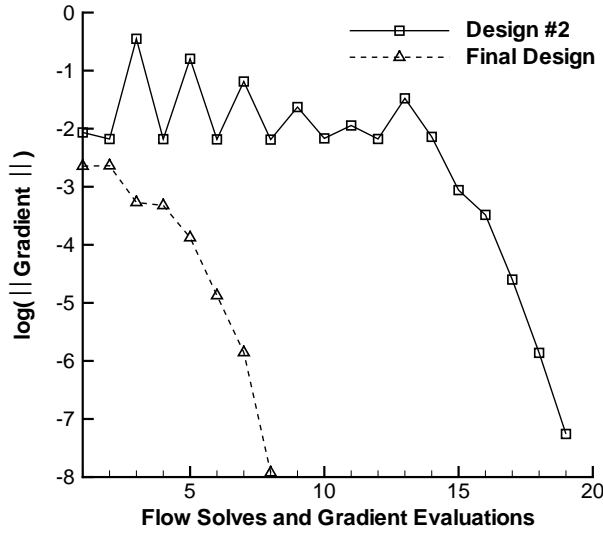


Fig. 7 Convergence histories for gap-overlap optimization

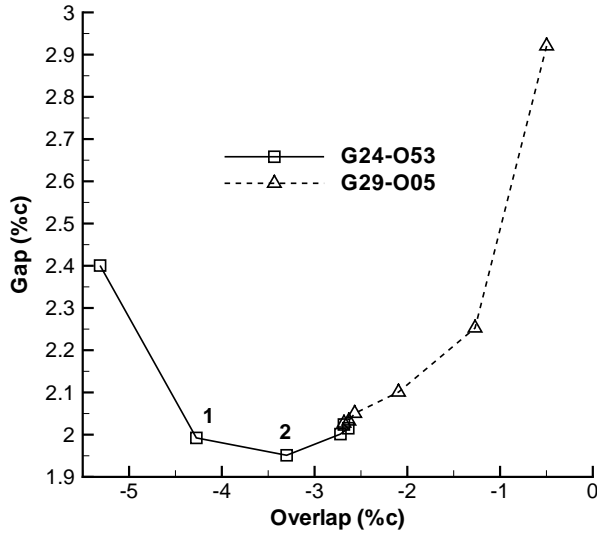


Fig. 8 Convergence to optimal gap-overlap distances from two distinct initial conditions

optimal solution, the optimization is restarted from a different initial condition. The flap is re-positioned to a gap of $2.9\%c$ and an overlap of $-0.5\%c$, i.e., the leading edge of the flap is almost aligned with the trailing edge of the main element. Fig. 8 shows that the optimization converges to the same optimum solution. The data labeled ‘G24-O53’ show the convergence to the optimum solution from the original configuration, with designs #1 and #2 indicated, while the data labeled ‘G29-O05’ show the convergence to the same optimum solution from the new initial conditions.

Multi-Objective Optimization

The performance of the Newton–Krylov algorithm is presented for the computation of a Pareto front that is based on two competing objective functions. In par-

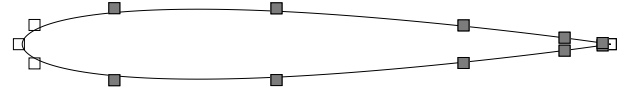


Fig. 9 B-spline control points and design variables (shaded control points) for the NACA 0012 airfoil

Table 3 Thickness constraints

T. C. no.	1	2	3
Location (%c)	25.0	92.0	99.0
Thickness (%c)	11.8	0.9	0.2

ticular, we consider the design of an airfoil shape to achieve specified lift and drag coefficients using the following two objectives:

$$\mathcal{J}_L = \left(1 - \frac{C_L}{C_L^*}\right)^2 \quad (18)$$

$$\mathcal{J}_D = \left(1 - \frac{C_D}{C_D^*}\right)^2 \quad (19)$$

The target lift and drag coefficients are chosen such that for a given set of design variables and constraints, the two objectives cannot be satisfied simultaneously. The objectives are competing, since a reduction in drag will typically result in a reduction in lift due to the decrease in the thickness and camber of the airfoil. Consequently, this problem does not have a unique solution. Instead, we seek to find a set of non-inferior solutions (referred to as a Pareto front) where an improvement in one of the objectives results in a degradation of the other.

There are numerous techniques to solve multi-objective problems.^{42,43} The technique used here is the weighted-sum method. The vector of the objective functions is converted to a scalar by assigning a weight to each objective and then forming a sum of the objectives. The resulting objective function is similar to Eq. 8 and is given by

$$\mathcal{J} = \omega_L \mathcal{J}_L + (1 - \omega_L) \mathcal{J}_D + \omega_T \sum_{j=1}^{N_c} C_j \quad (20)$$

where $\omega_T = 1.0$.

The results are presented for the following transonic design example. The freestream conditions are $M_\infty = 0.7$ and $Re = 9 \times 10^6$. We specify a target lift coefficient of 0.55 and a target drag coefficient of 0.0095. The initial airfoil is the NACA 0012 airfoil. The airfoil shape is described with 15 B-spline control points and we use 10 control points as design variables, as shown in Fig. 9. The angle of attack is also a design variable, resulting in a total of 11 design variables. In addition, we specify three thickness constraints as summarized in Table 3.

The computed Pareto front is shown in Fig. 10, where the trade-off between the competing objectives

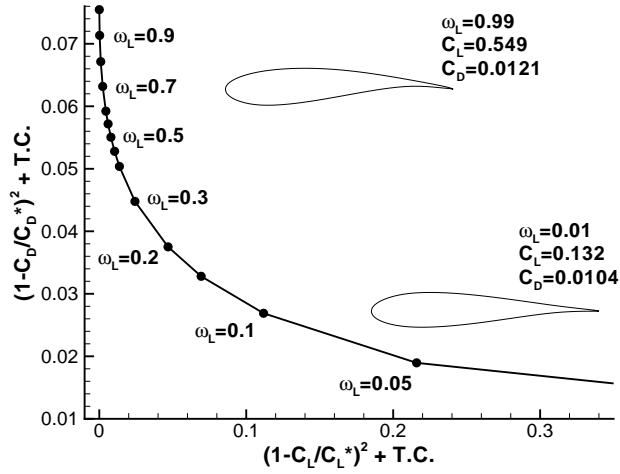


Fig. 10 Pareto front

Table 4 Aerodynamic coefficients for selected Pareto optimal solutions

ω_L	C_L	C_D	α
0.9	0.5440	0.01204	0.264
0.7	0.5291	0.01187	0.222
0.5	0.5074	0.01169	0.167
0.3	0.4693	0.01145	0.0906
0.1	0.3681	0.01099	-0.0557

is clearly captured. The label “T.C.” denotes the thickness-constraint penalty value. Also shown are two sample airfoil shapes obtained at the end-points of the front. Aerodynamic coefficients for a few selected solutions are provided in Table 4.

In order to ensure that an optimum solution is attained for each value of ω_L , we require a reduction of at least three orders of magnitude in the L_2 norm of the gradient. Example convergence histories are shown in Fig. 11. The first optimum solution is obtained for $\omega_L = 0.9$, which requires approximately 130 flowfield and gradient evaluations. The oscillations in the L_2 norm of the gradient are mainly due to the activation of thickness constraints during the line-search procedure. The solutions for the remaining values of ω_L are computed in decreasing order by warm-starting the optimization from the previous solution. The warm-started solutions are typically obtained in 65 to 90 flowfield and gradient evaluations, as indicated in Fig. 11. An example convergence history of the objective function is shown in Fig. 12 for $\omega_L = 0.9$. The values of the objective function are plotted at the end of each search direction, i.e., when the line-search exit criteria are satisfied. Note that within 25 flowfield and gradient evaluations, the objective function is converged to engineering accuracy.

Since the Pareto front shown in Fig. 10 has been obtained using a gradient-based method, the convergence to a true, or global, Pareto front is not guaranteed. In

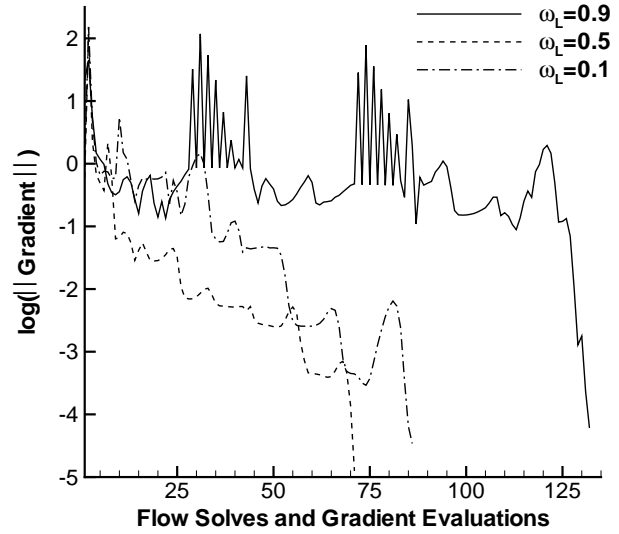


Fig. 11 Gradient convergence histories for selected Pareto front solutions

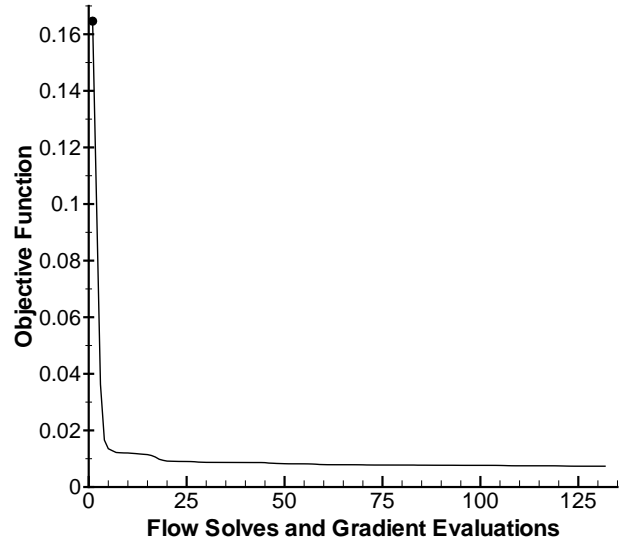


Fig. 12 Objective function convergence history for $\omega_L = 0.9$

order to investigate whether a global front has been captured, we solve this multi-objective problem using a genetic algorithm developed by Holst and Pulliam.¹⁰ Note that the Newton–Krylov algorithm and the genetic algorithm use identical spatial discretization of the flow equations, objective functions and constraints, as well as design variables.

The results are summarized in Fig. 13, where we show the original, gradient-based, front labeled as “Gradient”, and a front computed by the genetic algorithm using a dominance-based approach,⁴² labeled as “GA”. The dominance-based approach is specifically designed to capture global Pareto fronts; however, its computational cost is greater when compared to other techniques. Using the genetic algorithm, the Pareto front is obtained in 150 generations, which requires

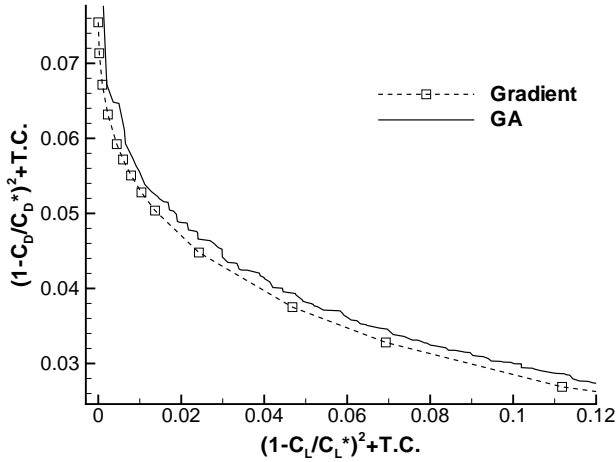


Fig. 13 Comparison of Pareto fronts obtained using the gradient and genetic algorithms

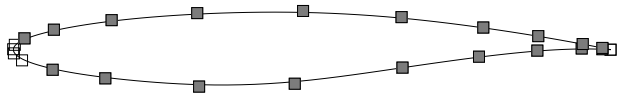


Fig. 14 B-spline control points and design variables (shaded control points) for the RAE 2822 airfoil

approximately 3000 flowfield evaluations. Overall, the genetic algorithm results confirm that the gradient-based front is a global Pareto front. Furthermore, it is well known that genetic algorithms exhibit slow convergence rates when close to an optimum solution. This is indicated in Fig. 13, where slightly better results are obtained by the Newton–Krylov algorithm.

Multi-Point Optimization

In order to investigate the performance of the Newton–Krylov algorithm for multi-point optimization problems, the design of a low-drag airfoil for transonic flight conditions at a specified lift coefficient is considered. This example is based on one of the cases studied by Drela.²³ The objective function is given by Eq. 4, where the target drag coefficient, C_D^* , is set to 0.013, the target lift coefficient, C_L^* , is set to 0.733, and the Reynolds number is 2.88×10^6 . The initial airfoil is the RAE 2822 airfoil. The airfoil shape is described with 25 control points and we use 19 control points as design variables, as well as the angle of attack. The B-spline control points together with the active design variables are shown in Fig. 14. The values of ω_L and ω_D are set 1.0 and 0.1, respectively. In addition, three airfoil thickness constraints are specified, as summarized in Table 5. The constraint at 35% c represents the initial airfoil thickness, while the constraints near the trailing edge are used to prevent airfoil surface cross-over. The value of ω_T is set to 1.0.

T. C. no.	1	2	3
Location (% c)	35.0	96.0	99.0
Thickness (% c)	12.04	0.5	0.12

Table 5 Thickness constraints

First, we consider a single-point optimization problem for the design Mach number of 0.74. Fig. 15(a) shows the initial and final pressure distributions and the corresponding airfoil shapes. Fig. 15(b) shows the values of the drag coefficient over a range of Mach numbers for $C_L = 0.733$. The drag coefficient is reduced by 36.4% at the design Mach number. The final thickness at 35% c is 12.0% c , which is very close to the desired thickness. However, for Mach numbers below 0.71 the optimized airfoil performs significantly worse than the original airfoil.

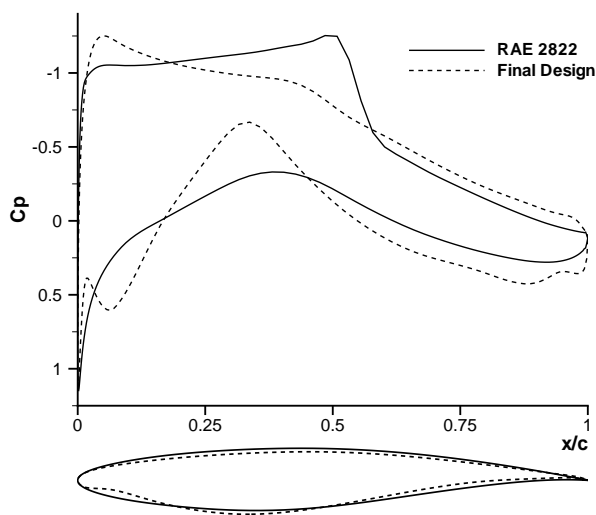
Next, we consider a four-point optimization problem where the design Mach numbers are 0.68, 0.71, 0.74 and 0.76. The weights assigned to each design Mach number for the weighted-sum method, Eq. 5, are 1.0, 1.0, 2.0 and 3.0, respectively. Fig. 16(a) shows the initial and final pressure distributions and the corresponding airfoil shapes for the design point $M = 0.74$. Fig. 16(b) shows the values of the drag coefficient over a range of Mach numbers for $C_L = 0.733$. When compared with the initial RAE 2822 airfoil, the new design achieves significantly lower drag values for Mach numbers above 0.71. The drag-divergence Mach number is increased by 7.0%. The drag coefficient is reduced by 33.8% at $M = 0.74$, which is only slightly less than the reduction obtained for the single-point optimization problem. Although the resulting airfoil is not suitable for practical use, with judicious definition of objectives and constraints for a specific application, the Newton–Krylov algorithm can provide realistic designs.

Conclusions

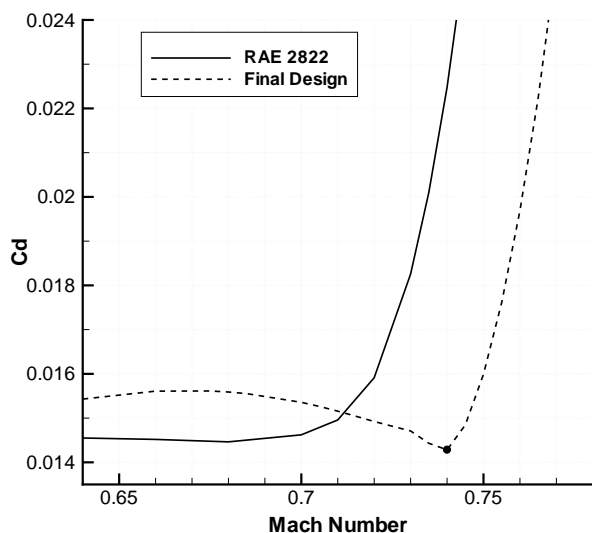
A Newton–Krylov algorithm for the design of single- and multi-element airfoil configurations has been presented. The accuracy of the objective function gradient, based on the discrete-adjoint method, is excellent. Furthermore, the gradient is obtained in approximately one-fifth of the flow solve time. The design examples demonstrate that the new algorithm provides an effective approach for aerodynamic design problems with multiple objectives and operating points. Future work should concentrate on more detailed comparisons between the gradient-based and genetic algorithms for complex multi-objective problems. In addition, the capabilities of the new algorithm need to be investigated for practical design problems with more complex objectives and constraints (preferably defined by industry experts).

Acknowledgments

This research was supported by the Natural Sciences and Engineering Research Council of Canada,

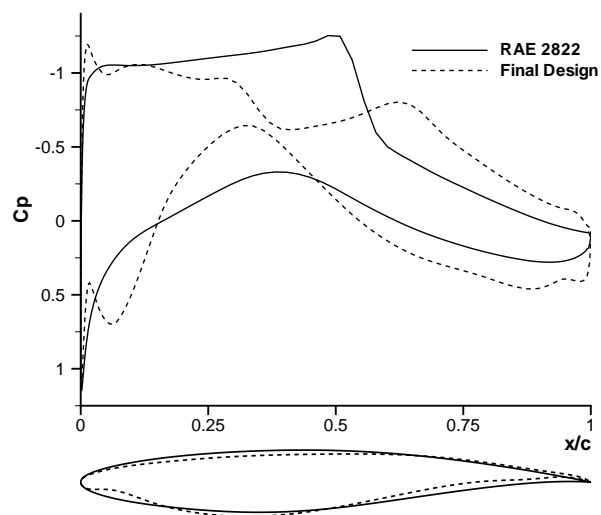


a) Pressure distribution and airfoil shapes ($M = 0.74$)

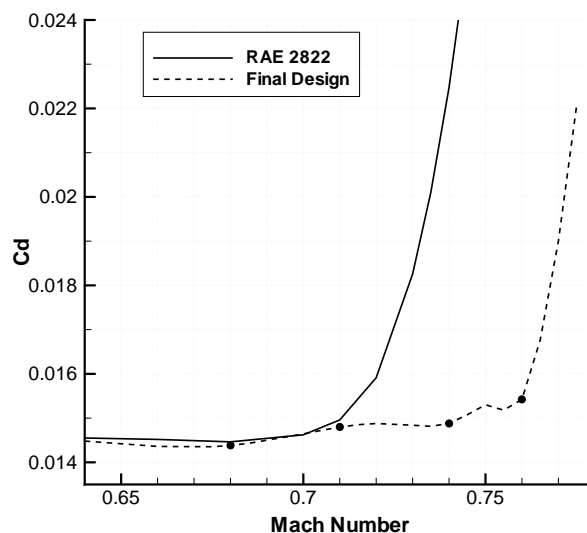


b) Drag coefficient at $C_L = 0.733$

Fig. 15 Single-point optimization



a) Pressure distribution and airfoil shapes ($M = 0.74$)



b) Drag coefficient at $C_L = 0.733$

Fig. 16 Four-point optimization

as well as Bombardier Aerospace and an OGS grant from the Government of Ontario. The authors gratefully acknowledge Samy Elias for his assistance with the multi-point design cases.

References

- ¹Rumsey, C. L. and Ying, S. X., "Prediction of High Lift: Review of Present CFD Capability," *Progress in Aerospace Sciences*, Vol. 38, No. 2, 2002, pp. 145–180.
- ²Jameson, A., Pierce, N. A., and Martinelli, L., "Optimum Aerodynamic Design using the Navier-Stokes Equations," *Theoretical and Computational Fluid Dynamics*, Vol. 10, No. 1, 1998, pp. 213–237.
- ³Soemarwoto, B. I. and Labrujère, T. E., "Airfoil Design and Optimization Methods: Recent Progress at NLR," *International Journal for Numerical Methods in Fluids*, Vol. 30, No. 2, 1999, pp. 217–228.
- ⁴Anderson, W. K. and Bonhaus, D. L., "Airfoil Design on Unstructured Grids for Turbulent Flows," *AIAA Journal*, Vol. 37, No. 2, 1999, pp. 185–191.
- ⁵Nielsen, E. J. and Anderson, W. K., "Aerodynamic Design Optimization on Unstructured Meshes Using the Navier Stokes Equations," *AIAA Journal*, Vol. 37, No. 11, 1999, pp. 1411–1419.
- ⁶Kim, C. S., Kim, C., and Rho, O. H., "Sensitivity Analysis for the Navier-Stokes Equations with Two-Equation Turbulence Models," *AIAA Journal*, Vol. 39, No. 5, 2001, pp. 838–845.
- ⁷Giles, M. B., Duta, M. C., and Müller, J.-D., "Adjoint Code Developments Using the Exact Discrete Approach," AIAA Paper 2001–2596, June 2001.
- ⁸Obayashi, S., "Aerodynamic Optimization with Evolutionary Algorithms," *Inverse Design and Optimization Methods, Lecture Series 1997-05*, edited by R. A. V. den Braembussche and M. Manna, von Kármán Institute for Fluid Dynamics, Brussels, Belgium, 1997.
- ⁹Giannakoglou, K. C., "Design of optimal aerodynamic shapes using stochastic optimization methods and computa-

- tional intelligence," *Progress in Aerospace Sciences*, Vol. 38, No. 1, 2002, pp. 43–76.
- ¹⁰Holst, T. L. and Pulliam, T. H., "Aerodynamic Shape Optimization Using a Real-Number-Encoded Genetic Algorithm," AIAA Paper 2001–2473, June 2001.
- ¹¹Hicks, R. M., Murman, E. M., and Vanderplaats, G. N., "An Assessment of Airfoil Design by Numerical Optimization," Tech. rep., NASA TM X-3092, July 1974.
- ¹²Elliott, J. and Peraire, J., "Constrained, Multipoint Shape Optimisation for Complex 3D Configurations," *Aeronautical Journal*, Vol. 102, No. 1017, 1998, pp. 365–376.
- ¹³Tse, D. and Chan, L., "Transonic Airfoil Design Optimization Using Soft Computing Methods," *Canadian Aeronautics and Space Journal*, Vol. 46, No. 2, June 2000, pp. 65–73.
- ¹⁴Reuther, J. J., Alonso, J. J., Rimlinger, M. J., and Jameson, A., "Aerodynamic Shape Optimization of Supersonic Aircraft Configurations via an Adjoint Formulation on Distributed Memory Parallel Computers," *Computers & Fluids*, Vol. 28, 1999, pp. 675–700.
- ¹⁵Nadarajah, S. K., Jameson, A., and Alonso, J. J., "An Adjoint Method for the Calculation of Remote Sensitivities in Supersonic Flow," AIAA Paper 2002–0261, Jan. 2002.
- ¹⁶Eyi, S., Lee, K. D., Rogers, S. E., and Kwak, D., "High-Lift Design Optimization Using Navier-Stokes Equations," *Journal of Aircraft*, Vol. 33, No. 3, 1996, pp. 499–504.
- ¹⁷Greenman, R. M., "Two-Dimensional High-Lift Optimization Using Neural Networks," NASA TM-1998–112233, June 1998.
- ¹⁸Alexandrov, N. M., Nielsen, E. J., Lewis, R. M., and Anderson, W. K., "First-Order Model Management with Variable-Fidelity Physics Applied to Multi-Element Airfoil Optimization," AIAA Paper 2000–4886, September 2000.
- ¹⁹Nielsen, E. J. and Anderson, W. K., "Recent Improvements in Aerodynamic Design Optimization on Unstructured Meshes," *AIAA Journal*, Vol. 40, No. 6, 2002, pp. 1155–1163.
- ²⁰Kim, S., Alonso, J. J., and Jameson, A., "Design Optimization of High-Lift Configurations Using a Viscous Continuous Adjoint Method," AIAA Paper 2002–0844, Jan. 2002.
- ²¹van Dam, C. P., "The aerodynamic design of multi-element high-lift systems for transport airplanes," *Progress in Aerospace Sciences*, Vol. 38, No. 2, 2002, pp. 101–144.
- ²²Martins, J. R. R. A., Alonso, J. J., and Reuther, J. J., "High-Fidelity Aero-Structural Design Optimization of a Supersonic Business Jet," AIAA Paper 2002–1483, April 2002.
- ²³Drela, M., "Pros & Cons of Airfoil Optimization," *Frontiers of Computational Fluid Dynamics 1998*, edited by D. A. Caughey and M. M. Hafez, World Scientific, Singapore, 1998, pp. 363–381.
- ²⁴Huyse, L. and Lewis, R. M., "Aerodynamic Shape Optimization of Two-dimensional Airfoils Under Uncertain Conditions," NASA CR-2001–210648, Jan. 2001, Also ICASE Report No. 2001–1.
- ²⁵Nemec, M. and Zingg, D. W., "Newton-Krylov Algorithm for Aerodynamic Design Using the Navier-Stokes Equations," *AIAA Journal*, Vol. 40, No. 6, 2002, pp. 1146–1154.
- ²⁶Saad, Y. and Schultz, M. H., "GMRES: A Generalized Minimal Residual Algorithm for Solving Nonsymmetric Linear Systems," *SIAM Journal on Scientific and Statistical Computing*, Vol. 7, No. 3, 1986, pp. 856–869.
- ²⁷Farin, G. E., *Curves and Surfaces for Computer-Aided Geometric Design: A Practical Guide*, Academic Press, San Diego, 4th ed., 1997.
- ²⁸Van Den Berg, B., "Boundary Layer Measurements on a Two-Dimensional Wing with Flap," NLR TR 79009 U, Jan. 1979.
- ²⁹Pulliam, T. H., "Efficient Solution Methods for the Navier-Stokes Equations," Tech. rep., Lecture Notes for the von Kármán Inst. for Fluid Dynamics Lecture Series: Numerical Techniques for Viscous Flow Computation in Turbomachinery Buildings, Brussels, Belgium, Jan. 1986.
- ³⁰Spalart, P. R. and Allmaras, S. R., "A One-Equation Turbulence Model for Aerodynamic Flows," AIAA Paper 92–0439, Jan. 1992.
- ³¹Nocedal, J. and Wright, S. J., *Numerical Optimization*, Springer-Verlag Inc., New York, 1999.
- ³²Nelson, T. E., Zingg, D. W., and Johnston, G. W., "Compressible Navier-Stokes Computations of Multielement Airfoil Flows Using Multiblock Grids," *AIAA Journal*, Vol. 32, No. 3, 1994, pp. 506–511.
- ³³Godin, P., Zingg, D. W., and Nelson, T. E., "High-Lift Aerodynamic Computations with One- and Two-Equation Turbulence Models," *AIAA Journal*, Vol. 35, No. 2, 1997, pp. 237–243.
- ³⁴Pueyo, A. and Zingg, D. W., "Efficient Newton-Krylov Solver for Aerodynamic Computations," *AIAA Journal*, Vol. 36, No. 11, 1998, pp. 1991–1997.
- ³⁵Chow, E. and Saad, Y., "Experimental Study of ILU Preconditioners for Indefinite Matrices," *Journal of Computational and Applied Mathematics*, Vol. 86, 1997, pp. 387–414.
- ³⁶Gunzburger, M. D., "Introduction into Mathematical Aspects of Flow Control and Optimization," *Inverse Design and Optimization Methods*, 1997–05, von Kármán Institute For Fluid Dynamics, Brussels, Belgium, April 1997.
- ³⁷Giles, M. B. and Pierce, N. A., "An Introduction to the Adjoint Approach to Design," *Flow, Turbulence and Combustion*, Vol. 65, No. 3/4, 2000, pp. 393–415.
- ³⁸Giles, M. B. and Pierce, N. A., "Analytic Adjoint Solutions for the Quasi-One-Dimensional Euler Equations," *Journal of Fluid Mechanics*, Vol. 426, 2001, pp. 327–345.
- ³⁹Reuther, J. J., Jameson, A., Alonso, J. J., Rimlinger, M. J., and Saunders, D., "Constrained Multipoint Aerodynamic Shape Optimization Using an Adjoint Formulation and Parallel Computers, Part 2," *Journal of Aircraft*, Vol. 36, No. 1, 1999, pp. 61–74.
- ⁴⁰Nielsen, E. J., *Aerodynamic Design Sensitivities on an Unstructured Mesh Using the Navier Stokes Equations and a Discrete Adjoint Formulation*, Ph.D. thesis, Virginia Polytechnic Institute and State University, 1998.
- ⁴¹Kim, H.-J., Sasaki, D., Obayashi, S., and Nakahashi, K., "Aerodynamic Optimization of Supersonic Transport Wing Using Unstructured Adjoint Method," *AIAA Journal*, Vol. 39, No. 6, 2001, pp. 1011–1020.
- ⁴²Coello, C. A. C., "A Comprehensive Survey of Evolutionary-Based Multiobjective Optimization Techniques," *Knowledge and Information Systems*, Vol. 1, No. 3, 1999, pp. 269–308, also see www.lania.mx/~ccoello/EMOO/EMOObib.html.
- ⁴³Marco, N., Désidéri, J.-A., and Lanteri, S., "Multi-Objective Optimization in CFD by Genetic Algorithms," Tech. Rep. 3686, Institut National De Recherche En Informatique Et En Automatique (INRIA), France, April 1999, also see www.lania.mx/~ccoello/EMOO/EMOObib.html.